Nonlinear vibration isolation via a compliant mechanism and wire ropes

Mu-Qing Niu · Li-Qun Chen

Abstract Nonlinear vibration isolation systems with both stiffness and damping nonlinearities are promising for a broad-band and high-efficient isolation performance. In this research, a novel nonlinear isolator is proposed via a compliant mechanism with negative stiffness and wire ropes with hysteretic damping. The compliant mechanism consists of two pairs of tilted flexure beams, and the nonlinear restoring force is modelled based on a beam constraint model. The hysteretic restoring force of the wire ropes is characterized by a Bouc–Wen model. A dynamic model of the nonlinear isolator is established, and a semi-analytical method is adopted to analyze the model. Generalized equivalent stiffness and a generalized equivalent damping ratio are defined, respectively, for dynamic systems with multiple nonlinearities. The compliant mechanism exhibits negative stiffness in a limited stroke and endows the isolator with a lower resonant frequency and a smaller resonant amplitude. The complaint mechanism with a symmetric restoring force is more preferred for a broader band of vibration isolation and fewer harmonics in the responses. The wire ropes improve the high-frequency isolation efficiency at the cost of a higher resonant frequency. The incorporation of the compliant mechanism and the wire ropes is beneficial for vibration isolation. Furthermore, the influences of the dimensions of the complaint mechanism on the negative-stiffness stroke, load capacity and vibration isolation performances of the nonlinear isolator are revealed.

1 Introduction

Nonlinear vibration isolation systems [1–5] have shown great promise in broad-band and high-efficient vibration isolation performances. An isolation system with high-static-low-dynamic-stiffness (HSLDS) characteristics exhibits a low resonant frequency without large static deflections. Thus the low-frequency vibration isolation is enhanced. An isolation system with nonlinear damping can effectively suppress the resonances without deteriorating the high-frequency vibration isolation provided that the nonlinear damping is appropriately designed. Investigations on nonlinear vibration isolators have drawn considerable attentions.

Generally, an HSLDS system is composed of a positive-stiffness element and a negative-stiffness element [6]. The positive-stiffness element enhances

M.-Q. Niu · L.-Q. Chen (✉)
School of Science, Harbin Institute of Technology,
Shenzhen 518055, China
e-mail: chenliqun@hit.edu.cn

the stability and the load-bearing capacity of the system, and the element is usually in the form of coil springs. The negative-stiffness element reduces the dynamic stiffness of the system and can be facilitated by pre-deformed springs [7–11], pre-bulked beams [12–16], convexities [17, 18] and magnetics [19, 20]. The three-spring structure is the most studied model with the negative stiffness resulting from two horizontal/oblique pre-compressed springs. Lu et al. [9] extended the structure to a two-stage vibration isolation system. Gatti [11] modified the three-spring structure with four oblique pre-compressed springs. Elastic beams present negative stiffness when compressed beyond their buckling loads. Liu et al. [12] proposed a negative-stiffness corrector formed by a pair of Euler buckled beams. Yan et al. [16] investigated an anti-spring isolator consisting of several quasi-trapezoidal blade springs. Cheng et al. [17] and Zhou et al. [18] proposed vibration isolators via cam-roller mechanisms, and the negative stiffness is derived from the geometric constraints of the convexities. The magnetic force between two magnets is inversely proportional to the square of the distance. Based on the theory, Shi et al. [19] and Wang et al. [20] proposed negative-stiffness elements with permanent magnets and electromagnets, respectively. In order to produce the negative stiffness, the elements must be with stored elastic potential energy or magnetic energy at their initial states. The structures are usually intentionally pre-deformed and sometimes with large internal stress. Thus, precision assemblies are essential and difficult for the HSLDS devices. The gaps, asymmetries and frictions due to the assembly errors and the relative movements of the connectors significantly influence the performances of the devices. The difficulty in precision assembly is one of the limitations for the HSLDS devices applying to scaled structures or systems.

Compliant mechanisms realize motions through elastic deformations of the materials with the advantages of no gap and no friction [21]. A compliant mechanism can be manufactured as a whole through wire electrical-discharge machining, and thus the problems in precision assembly are avoided. The generation of the nonlinear stiffness highly depends on the storage and the release of the potential energy. Gatti [22] presented an analytical insight on a K-shaped spring configuration for the purpose of elastic potential energy maximum. A compliant mechanism stores elastic potential energy through the deformations of the whole flexure structure instead of distributed springs, and negative stiffness can be produced with deliberately designed structure and dimensions. Xu [23] proposed a tilted-angle parallelogram flexure mechanism with the negative stiffness presented in a large stroke. Han et al. [24] investigated a double-tensural fully-compliant mechanism with negative stiffness, and all the compliant segments are loaded in tension without buckling problems. Zhao et al. [25] analyzed a rotational flexure pivot with quasi-zero stiffness. The force–displacement relation of a negative-stiffness mechanism is nonlinear and can be predicted by the beam constraint model (BCM) [26] and the power series method [27]. However, in the existing literature, the negative stiffness is usually a by-product of the multi-stable compliant mechanism, and the mechanism is designed for kinetic purposes such as constant-force and static-balancing. The research limits to the snap-through properties [28, 29] and the kinetic designs [30, 31]. There is little research on the dynamic characteristics of the negative-stiffness compliant mechanisms and their performances for vibration isolation. Furthermore, parallel structures are extensively used in compliant mechanisms for kinetic applications, while their applicability in dynamics remains unknown.

Vibration isolation performances of HSLDS systems can be further improved by introducing nonlinear damping such as the nonlinear viscous damping and the hysteretic damping. Nonlinear damping can be produced from geometric nonlinearities [32], materials with intrinsic nonlinearities [33], viscous fluids [34] and frictions [35]. Among them, wire ropes exhibit hysteretic damping due to inner frictions, and the structure is simple and practical for engineering applications. Wire ropes have been adopted in vibration control as Stockbridge dampers [36] and ring-type springs [37]. Carpineto et al. [38] adopted wire ropes with both ends clamped for vibration mitigation, and the stiffness softening/hardening characteristics were observed. Carboni et al. [39, 40] improved the structure by introducing NiTiNOL for larger energy dissipation, and the pinching effects were revealed. Leblouba et al. [41] studied the shear cyclic behaviors of twelve polycal wire rope isolators through experiments, and proposed a Bouc–Wen–Baber–Noori model to characterize the hysteresis. Zhang et al. [42] introduced a NiTiNOL-steel wire rope into a

nonlinear energy sink to enhance the energy dissipation. Zheng et al. [43] integrated a NiTiNOL-steel wire rope with a composite laminated beam for structural vibration suppression. It is promising to incorporate the wire ropes into the HSLDS system to enhance the energy dissipation. The performances of a HSLDS vibration isolator incorporated by Bouc–Wen-type hysteretic damping has not been fully understood. There are theoretical and practical motivations to explore the stiffness-varying characteristics and the frequency responses of the incorporated isolator.

In this work, a nonlinear vibration isolator is proposed with the negative stiffness facilitated by a compliant mechanism and the hysteretic damping induced from wire ropes. The restoring forces of the nonlinear elements are characterized. The dynamic model of the nonlinear isolator is established and analyzed. Generalized equivalent stiffness and a generalized equivalent damping ratio are respectively defined to understand comprehensively the isolators with multiple nonlinearities. Comparison investigations demonstrate the merits in dynamic properties of the negative-stiffness structures and the effectiveness of the incorporation of different nonlinear elements.

The manuscript is organized as follows. Section 2 develops a model for the nonlinear restoring forces of the compliant mechanism and the wire ropes. Section 3 presents the dynamic model of the nonlinear isolator and the analysis methodology. Section 4 focuses on the comparisons of the nonlinear isolators with different structures. Section 5 performs parameter analysis. Section 6 ends the work with conclusions.

2 Modelling of the restoring forces

2.1 The restoring force of the compliant mechanism

Figure 1 shows the structure of a compliant mechanism presenting negative stiffness. The mechanism is
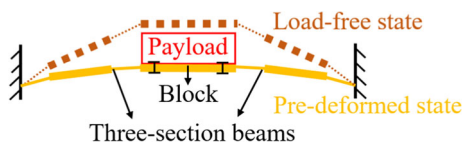

Fig. 1 The load-free and pre-deformed states of the up-tilted compliant mechanism

composed of two three-section beams and a block. The block is regarded as rigid and fixed on the payload. The three-section beam is composed of two thin beams for large deformations and one thick beam as a reinforcement. A small external force is enough to drive the structure into a post-buckling state, and the post-buckling is the basis of negative stiffness. The structure is widely used in bi-stable compliant mechanisms [27]. The load-free state is shown as dotted lines and the beams are up-tilted. At the balancing position for vibration isolation, the compliant mechanism is pre-deformed with stored elastic potential energy. Due to the symmetric structure, the payload and the block are only able to move vertically.

Consider a three-section cantilever beam shown in Fig. 2a. The load-free state is shown in dashed lines, and each beam is straight with a rectangular section. The length, the tilt angle, the out-of-plane width, the in-plane thickness and the moment of inertial of the ith beam are denoted as L_i, α_i, W_i, T_i and I_i, respectively. The Young's modulus of the beam is denoted as E. The deformed state is shown in solid lines. Elastic deformations occur under external loads (denoted as F_x, F_y and M_z) applied on the free end of the three-section beam. The horizontal displacement, the vertical displacement and the rotation angle of the free end are denoted as D_x, D_y and θ, respectively.

Each beam is regarded as a cantilever beam and analyzed according to its local coordinate. The elastic deformation of the ith beam is shown in Fig. 2b. The equivalent external loads applied on the ith beam are denoted as F_{ix}, F_{iy} and M_{iz}, respectively. The in-plane displacements of the free end are denoted as D_{ix}, D_{iy} and θ_i according to the local coordinate. Dimensionless parameters are introduced as

$$t_i = \frac{T_i}{L_i}, \quad d_{ix} = \frac{D_{ix}}{L_i}, \quad d_{iy} = \frac{D_{iy}}{L_i}, \quad f_{ix} = \frac{F_{ix}L_i^2}{EI_i}, \quad f_{iy} = \frac{F_{iy}L_i^2}{EI_i}, \quad m_{iz} = \frac{M_{iz}L_i}{EI_i}$$

$$(1)$$

According to the BCM [44], there areccording to the local coordinate. Dimensio

$$\begin{bmatrix} f_{iy} \\ m_{iz} \end{bmatrix} = \mathbf{p}_1 \begin{bmatrix} d_{iy} \\ \theta_i \end{bmatrix} + f_{ix}\mathbf{p}_2 \begin{bmatrix} d_{iy} \\ \theta_i \end{bmatrix} + f_{ix}^2 \mathbf{p}_3 \begin{bmatrix} d_{iy} \\ \theta_i \end{bmatrix} \qquad (2)$$

Fig. 2 The elastic deformations of the cantilever beams: **a** the three section beam **b** the ith beam

(a) the three-section beam

(b) the ith beam
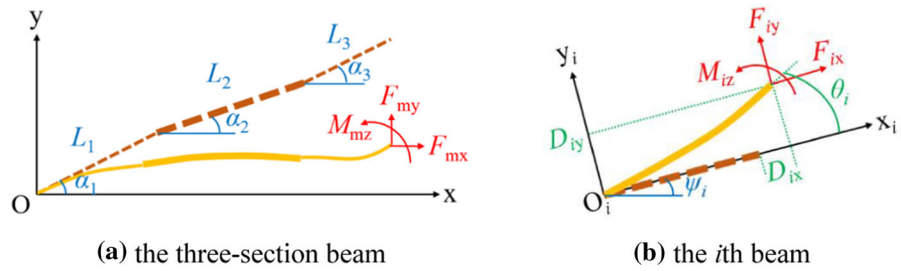
$$d_{ix} = \frac{f_{ix}t_i^2}{12} - \frac{1}{2}\begin{bmatrix} d_{iy} & \theta_i \end{bmatrix}\mathbf{p}_2\begin{bmatrix} d_{iy} \\ \theta_i \end{bmatrix}$$
$$- f_{ix}\begin{bmatrix} d_{iy} & \theta_i \end{bmatrix}\mathbf{p}_3\begin{bmatrix} d_{iy} \\ \theta_i \end{bmatrix} \qquad (3)$$

where

$$\mathbf{p}_1 = \begin{bmatrix} 12 & -6 \\ -6 & 4 \end{bmatrix}, \qquad \mathbf{p}_2 = \begin{bmatrix} 6/5 & -1/10 \\ -1/10 & 2/15 \end{bmatrix},$$
$$\mathbf{p}_3 = \begin{bmatrix} -1/700 & 1/1400 \\ 1/1400 & -11/6300 \end{bmatrix}$$

Equations (2) and (3) quantify the elastic deformations of the ith beam according to the local coordinate. The angle between the ith local coordinate and the global coordinate is denoted as ψ_i and expressed as

$$\psi_i = \alpha_i + \sum_{j=1}^{i-1} \theta_j \qquad (4)$$

According to the force equilibrium relation at the deformed state, there is

$$\begin{bmatrix} \cos\psi_i & -\sin\psi_i & 0 \\ \sin\psi_i & \cos\psi_i & 0 \\ -D_{iy} & L_i + D_{ix} & 1 \end{bmatrix}\begin{bmatrix} F_{ix} \\ F_{iy} \\ M_{iz} \end{bmatrix}$$
$$= \begin{bmatrix} \cos\psi_{i-1} & -\sin\psi_{i-1} & 0 \\ \sin\psi_{i-1} & \cos\psi_{i-1} & 0 \\ 0 & 0 & 1 \end{bmatrix}\begin{bmatrix} F_{(i-1)x} \\ F_{(i-1)y} \\ M_{(i-1)z} \end{bmatrix} \qquad (5)$$

For the three-section beam, the external loads according to the global coordinate are expressed as

$$\begin{bmatrix} F_x \\ F_y \\ M_z \end{bmatrix} = \begin{bmatrix} \cos\psi_3 & -\sin\psi_3 & 0 \\ \sin\psi_3 & \cos\psi_3 & 0 \\ 0 & 0 & 1 \end{bmatrix}\begin{bmatrix} F_{3x} \\ F_{3y} \\ M_{3z} \end{bmatrix} \qquad (6)$$

The geometric constraints are derived based on the structure shown in Fig. 1. Due to the symmetric structure, the horizontal displacement of the free end is 0. Besides, the free end is fixed on the block, thus the rotation angle is also 0. The constraints lead to

$$\begin{bmatrix} D_x \\ D_y \\ \theta \end{bmatrix} = \sum_{i=1}^{3}\left(\begin{bmatrix} \cos\psi_i & -\sin\psi_i & 0 \\ \sin\psi_i & \cos\psi_i & 0 \\ 0 & 0 & 1 \end{bmatrix}\begin{bmatrix} L_i + D_{ix} \\ D_{iy} \\ \theta_i \end{bmatrix}\right.$$
$$\left. - L_i\begin{bmatrix} \cos\alpha_i \\ \sin\alpha_i \\ 0 \end{bmatrix}\right) = \begin{bmatrix} 0 \\ D_y \\ 0 \end{bmatrix}$$
$$\qquad (7)$$

Equations (1–7) make up the elastic deformation model for the three-section beam in the form of nonlinear algebra equations. A path-following procedure is performed to obtain the relation between the vertical force and the vertical displacement of the free end. The vertical displacement D_y is set as the incremental parameter and starts from 0 (load-free condition). With a determined vertical displacement, the vertical force F_y can be acquired by solving the nonlinear equations.

A typical force–displacement relation of the three-section beam is shown in Fig. 3. The structure presents the negative stiffness in a limited region denoted as the working region. The region starts from $(-D_{ya}, -F_{ya})$ and ends at $(-D_{yc}, -F_{yc})$. The mid-point of the working region in the displacement scale is $(-D_{yb}, -F_{yb})$, i.e., $D_{yb} = (D_{ya} + D_{yc})/2$. A new coordinate is attached to the mid-point. The vertical displacement and the vertical force of the three-section beam measured from the new origin are denoted as Y_T and F_T, respectively.

For the convenience of computation, the relation between F_T and Y_T is fitted into a polynomial function as

$$F_T = \sum_{i=1}^{n_k} K_{Ti}Y_T^i \qquad (8)$$

where K_{Ti} is the coefficient of the ith-order term, and the highest order is n_k. It should be noted that Eq. (8) presents a mathematical model rather than a physical
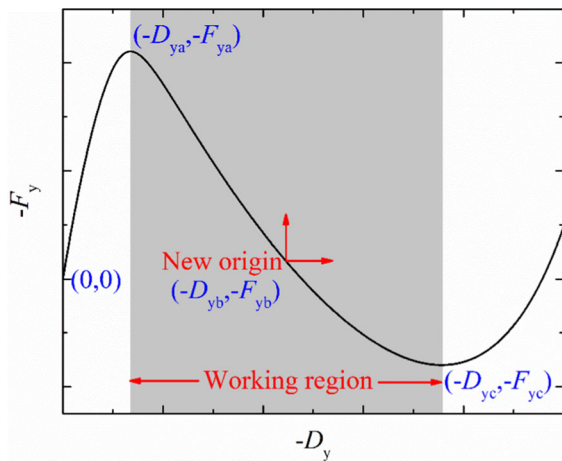
Fig. 3 The relation between the vertical force and the vertical displacement

model. Parameter K_{T1} indicates the initial stiffness at the new origin, while the high-order parameters K_{Ti} ($i = 2, 3, …, n_k$) have no physical meaning.

2.2 The restoring force of the wire ropes

The structure of the wire ropes with both ends clamped is shown in Fig. 4. The wire ropes exhibit nonlinear stiffness and hysteretic damping due to the inner frictions among the winded wires. Due to the symmetric structure, the payload is only able to move vertically. At the initial state, the wire ropes are horizontal without any residual hysteretic force. The gravity of the payload is ignored in this section because it is balanced by the linear spring the isolator.

The force–displacement relation of the wire rope is established with a semi-physical model. Firstly, the wire rope is assumed to be a cantilever beam with a constant section without inner friction. The length, the area of the section, the moment of inertial and the Young's modulus of the beam are denoted as L_w, A_w, I_w and E_w, respectively. The external loads applied on the free end of the beam are denoted as F_{wx}, F_{wy} and M_{wz}, respectively. The elastic deformations of the free end are denoted as X_w, Y_w and θ_w, respectively. At the initial state, the beam is horizontal with the axial force

Fig. 4 The wire ropes in a symmetric structure

denoted as F_{wx0} and the axial deformation denoted as X_{w0}. The geometric constraints indicate that the horizontal displacement $X_w = X_{w0}$, and the rotation angle θ_w is 0. Dimensionless parameters are introduced as

$$t_w = \sqrt{\frac{I_w}{L_w^2 A_w}}, \quad x_w = \frac{X_w}{L_w}, \quad y_w = \frac{Y_w}{L_w}, \quad x_{w0} = \frac{X_{w0}}{L_w},$$
$$f_{wx} = \frac{F_{wx}L_w^2}{E_w I_w}, \quad f_{wy} = \frac{F_{wy}L_w^2}{E_w I_w}, \quad f_{wx0} = \frac{F_{wx0}L_w^2}{E_w I_w} \tag{9}$$

where t_w is a characteristic dimension of the section, and for example, $t_w = D_w/(4L_w)$ for a circular section, where D_w is the diameter. According to the BCM [44], there are

$$f_{wy} = 12y_w + \frac{6}{5}f_{wx}y_w - \frac{1}{700}f_{wx}^2 y_w \tag{10}$$

$$x_w = f_{wx}t_w^2 - \frac{3}{5}y_w^2 + \frac{1}{700}f_{wx}y_w^2 \tag{11}$$

When $y_w < 8t_w$ (which is equal to $Y_w < 2D_w$ for a circular section), the third term on the right hand side of Eq. (11) is less than 1/10 of the first term, and thus it can be ignored for approximate calculation. At the initial state, there is only axial force and

$$x_{w0} = f_{wx0}t_w^2 \tag{12}$$

where x_{w0} and f_{wx0} are the initial axial deformation and the initial axial force, respectively. Based on the geometric constraints, there is $x_w = x_{w0}$. Subtracting Eq. (12) from Eq. (11) yields

$$f_{wx} = f_{wx0} + \frac{3y_w^2}{5t_w^2} \tag{13}$$

Substitute Eq. (13) into Eq. (10) and ignore the small-value terms. There is

$$f_{wy} = \left(12 + \frac{6f_{wx0}}{5} - \frac{f_{wx0}^2}{700}\right)y_w + \left(\frac{18}{25t_w^2} - \frac{3f_{wx0}}{1750t_w^2}\right)y_w^3 \tag{14}$$

According to Eq. (9), the dimensional form of Eq. (14) is

$$F_{wy} = \left(\frac{12E_w I_w}{L_w^3} + \frac{6F_{wx0}}{5L_w} - \frac{F_{wx0}^2 L_w}{700E_w I_w}\right)Y_w$$
$$+ \left(\frac{18E_w A_w}{25L_w^3} - \frac{3F_{wx0}A_w}{1750I_w L_w}\right)Y_w^3 \tag{15}$$

Equation (15) indicates the elastic force without the inner friction, and it contains a linear term and a cubic term due to the geometric nonlinearity.

Secondly, the inner frictions of the wire rope are characterized by a Bouc–Wen model [45], and the hysteretic force Z_w is expressed in a differential form:

$$Z'_w = \left\{ K_{wd} - \left[G + B\mathrm{sgn}\left(Y'_w Z_w\right)\right]|Z_w|^{n_b}\right\}Y'_w \qquad (16)$$

where K_d, G, B and n_b are the parameters of the Bouc–Wen model, and sgn denotes the signum function. As shown in [39, 40], the value of n_b is identified to be 1 exactly or approximately based on the experiments. A slight difference of n_b does not change the essential stiffness and damping characteristics of the wire ropes. Thus, for simplicity, the value of n_b is fixed as 1 in this work.

Finally, the total restoring force is the summation of the elastic force and the hysteretic force with an opposite direction. The total restoring force of the two wire ropes is expressed as

$$-F_w = K_{w1}Y + K_{w3}Y^3 + Z \qquad (17)$$

where

$$K_{w1} = \frac{24E_w I_w}{L_w^3} + \frac{12F_{wx0}}{5L_w} - \frac{F_{wx0}^2 L_w}{350 E_w I_w},$$

$$K_{w3} = \frac{36E_w A_w}{25 L_w^3} - \frac{3F_{wx0} A_w}{875 I_w L_w},$$

and F_w is the restoring force. The expression of Z is similar to Eq. (16) with $K_d = 2K_{wd}$.

The model parameters are identified based on the experimental data of the restoring forces in Reference [38]. In the experiments, a wire rope constituted by 7 strands of 19 steel wires is tested. The diameter of each wire is 0.65 mm and the length of the wire rope is 100 mm. With the section equivalent to a circular section with the same area, the equivalent diameter is about 7.5 mm. Thus, the proposed method is suitable for the conditions with Y_w within 15 mm. The identified parameters are shown in Table 1. It should be noted that K_{w1}, K_{w3} and K_d denote the corresponding stiffness coefficients with two wire ropes, while G and B are independent of the number of the wire ropes.

The calculation results and the experimental results of the restoring forces are shown in Fig. 5. The negative sign in the ordinate label indicates that the

Table 1 Identified parameters of the wire rope

$K_{w1}/2$	$K_{w3}/2$	$K_d/2$	G	B
5.52 N/mm	0.0357 N/mm^3	85.4 N/mm	0.87	4.57

direction of the restoring force is opposite to the deformation, and thus the slopes in the figure characterize the stiffness. The relative root mean square errors of the calculation results with the displacement amplitudes of 5 mm and 10 mm are 12.7% and 6.4%, respectively. The semi-physical model is not quantitatively accurate, while the shapes of the hysteretic loops are characterized. The model is accurate enough for the following dynamic analysis.

3 Dynamic model and analysis methods

3.1 Dynamic model of the isolator

The structure of the isolator with both the negative-stiffness compliant mechanism and the wire ropes is shown in Fig. 6. The payload is horizontally suspended by a pair of wire ropes, and vertically supported by a linear spring, a linear damper and the compliant mechanisms. The compliant mechanism is composed of an up-tilted part and a down-tilted part. The two parts are manufactured as a whole while pre-deformed in opposite directions. The payload and the middle block of the compliant mechanism are fixed together (Fig. 6). The linear spring increases the static stiffness and enhances the stability of the isolator. The linear damper increases the dissipated energy and is regarded as a comparison with the hysteretic damping.

In Fig. 6, the compliant mechanism includes four three-section beams, and the total restoring force is expressed as

$$-F_m = \sum_{i=1}^{n_k} K_{mi}Y^i \qquad (18)$$

where Y denotes the vertical relative displacement between the payload and the base, and F_m denotes the restoring force of the compliant mechanism.

Based on the restoring force models of the compliant mechanism [Eq. (18)] and the wire ropes [Eq. (17)], the dynamic model of the isolator can be
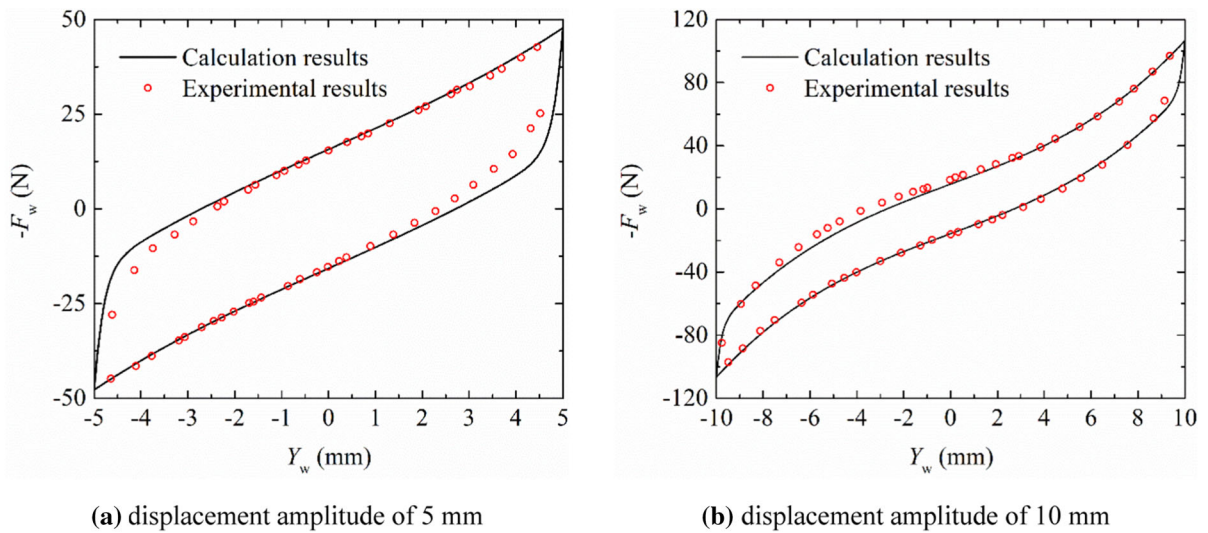
(a) displacement amplitude of 5 mm   **(b)** displacement amplitude of 10 mm

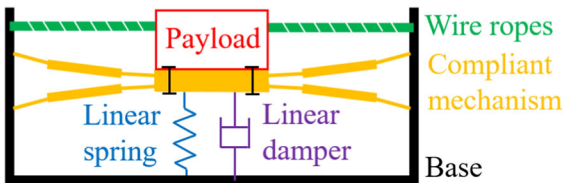**Fig. 5** The calculation and experimental [38] results of the restoring forces of the wire rope

Fig. 6 The structure of a nonlinear vibration isolator via compliant mechanisms and wire ropes

established. The stiffness of the linear spring is K_s, and the damping parameter of the linear damper is C. The mass of the payload is M. A harmonic displacement excitation is applied on the base in the vertical direction with the amplitude A_e and the frequency ω_e. The dynamic equation can be expressed as

$$MY'' + \sum_{i=1}^{n_k} K_i Y^i + CY' + Z = MA_e\omega_e\cos(\omega_e T)$$

$$(19)$$

$$Z' = \{K_d - [G + B\text{sgn}(Y'Z)]|Z|^{n_b}\}Y'$$

$$(20)$$

where

$$K_i = \begin{cases} K_{m1} + K_{w1} + K_s & (i=1) \\ K_{m3} + K_{w3} & (i=3) \\ K_{mi} & (\text{others}) \end{cases}$$

and T denotes the time. Introduction of dimensionless parameters leads to

$$\eta^2\ddot{y} + \sum_{i=1}^{n_k} k_i y^i + c\eta\dot{y} + \delta z = \eta^2\cos t$$

$$(21)$$

$$\dot{z} = \{1 - [\gamma + \beta\text{sgn}(\dot{y}z)]|z|^{n_b}\}\dot{y}$$

$$(22)$$

where

$$\begin{cases} \omega_c = \sqrt{\dfrac{K_c}{M}}, & \eta = \dfrac{\omega_e}{\omega_c}, & y = \dfrac{Y}{A_e}, & k_i = \dfrac{K_i A_e^{i-1}}{K_c}, & c = \dfrac{C\omega_c}{K_c}, \\ t = \omega_e T, & z = \dfrac{Z}{K_d A_e}, & \delta = \dfrac{K_d}{K_c}, & \gamma = GA_e^{n_b}K_d^{n_b-1}, & \beta = BA_e^{n_b}K_d^{n_b-1} \end{cases}$$

and K_c, Y_c and ω_c are the characteristic stiffness, the characteristic displacement and the characteristic frequency, respectively. The amplitudes of the absolute and relative payload displacements are denoted as A_p and A, respectively, and their dimensionless forms are $a_p = A_p/A_e$ and $a = A/A_e$, respectively. Thus, there is $T_D \equiv a_p$, where T_D is the displacement transmissibility.

The dynamic model is solved with a semi-analytical method introduced in our previous work [46]. A harmonic balance method (HBM) is used to transform the differential equations into nonlinear algebra equations. The Fourier expansions of the high-order terms in the polynomial function is obtained through a recursive method [46]. The implicit function of the Bouc–Wen model is dealt with an alternating frequency/time domain technique [47]. The nonlinear algebra equations are solved with a combination of the Levenberg–Marquardt method [48] and the arc-length continuation method [49]. The frequency responses

are acquired through a swept-frequency process. The stability of the periodic solution is analyzed based on the Floquet theory, and the transition matrix is calculated through a precise Hsu's method [50].

3.2 Generalized equivalent stiffness and generalized equivalent damping ratio

The nonlinear isolation system is further analyzed through the generalized equivalent stiffness and the generalized equivalent damping ratio [46]. The generalized equivalent stiffness is derived from the anhysteretic restoring force. According to the basic characteristics of the Bouc–Wen model, the anhysteretic Bouc–Wen force is defined as

$$\dot{z}_{an} = [1 - (\gamma + \beta)|z_{an}|]\dot{y} \tag{23}$$

where z_{an} is the anhysteretic Bouc–Wen force, and it equals 0 at $y = 0$. Integration of Eq. (23) leads to

$$z_{an} = \frac{\text{sgn}(y)}{\gamma + \beta}\left[1 - e^{-(\gamma+\beta)|y|}\right] \tag{24}$$

Hence the anhysteretic restoring force of the isolator is expressed as

$$-f_{r-an} = \sum_{i=1}^{n_k} k_i y^i + \delta \frac{\text{sgn}(y)}{\gamma + \beta}\left[1 - e^{-(\gamma+\beta)|y|}\right] \tag{25}$$

where $f_{r\text{-}an}$ is the anhysteretic restoring force, and the equivalent stiffness is

$$k_e = -\frac{df_{r-an}}{dy} = \sum_{i=1}^{n_k} ik_i y^{i-1} + \delta e^{-(\gamma+\beta)|y|} \tag{26}$$

where k_e is the equivalent stiffness of the isolator in the dimensionless form.

The generalized equivalent damping ratio is derived from the dissipated energy and the generalized stored elastic energy. The dimensionless amplitude of the relative displacement between the payload and the base is denoted as a. The dissipated energy in one period is expressed as

$$E_d = \int_a^{-a} f_r - \int_{-a}^a f_r \tag{27}$$

where f_r is the hysteretic restoring force and expressed as

$$-f_r = \sum_{i=1}^{n_k} k_i y^i + c\eta\dot{y} + \delta z \tag{28}$$

The maximum generalized stored energy is computed through the anhysteretic restoring force as

$$E_s = -\int_0^a f_{r-an} dy \tag{29}$$

It should be noted that E_d and E_s are both in the dimensionless form, and the equivalent damping ratio is defined by their ratio as

$$\zeta_e = \frac{E_d}{4\pi\eta E_s} \tag{30}$$

where ζ_e is the equivalent damping ratio.

4 Structure comparison

4.1 Structures of the compliant mechanisms

Figure 7 shows two nonlinear isolators with different structures of the compliant mechanism. In the parallel structure, the three-section beams are tilted in the same direction. The structure is easier for mounting and widely used for kinetic applications. In the symmetric structure, the three-section beams are tilted in opposite directions. The structure is proposed in this research to achieve a better dynamic performance.

The dimensions of the three-section beams are shown in Table 2. The total length is 100 mm, and it is

Fig. 7 Isolators with different structures of compliant mechanisms: **a** parallel structure **b** symmetric structure

(a) parallel structure   **(b)** symmetric structure
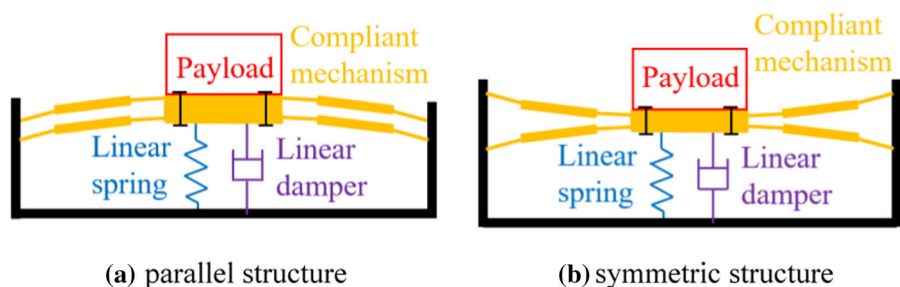
the same with the length of the wire ropes shown in Sect. 2.2. The tilting angles of the up-tilted and down-tilted beams are positive and negative, respectively. The absolute value of the tilting angle is selected as the maximum value with the maximum stress in the three-section beam below 800 MPa during deformation. The relation between the maximum tilting angle and the thickness of the beams will be discussed in Sect. 5. The restoring forces and the equivalent stiffness of the compliant mechanisms are shown in Fig. 8. Both the calculation results based on the BCM and the fitting results based on a 3-order polynomial function are demonstrated in Fig. 8a. The fitting results well coincide with the physical model within the working region, and the relative root mean square errors are within 3%. A finite element analysis (FEA) is performed with ANSYS to verify the physical model, and the results are shown as scatters in Fig. 8a. Compared with the FEA results, the root mean square errors of the BCM-based results are within 1%.

As shown in Fig. 8, the initial stiffness of the two structures are the same, and the working regions are also the same. The restoring force of the symmetric structure is symmetric about the origin. The minimum equivalent stiffness is −153.4 N/mm, and it appears at the initial state. The restoring force of the parallel structure is asymmetric, and the minimum equivalent stiffness is −169.1 N/mm.

The symmetric and parallel structures are adopted in nonlinear isolators and compared with a linear isolator. For the nonlinear isolator, the stiffness of the linear spring K_s equals the absolute value of the minimum equivalent stiffness of the compliant mechanism. Thus, the isolators are stable in static equilibrium states. For comparison, the linear spring in the linear isolator is the same with that in the nonlinear isolator with the symmetric structure. The characteristic stiffness and the excitation amplitude are $K_c = 153.4$ N/mm and $A_e = 1$ mm, respectively. The dimensionless stiffness parameters are shown in Table 3.

The frequency responses of three isolators are shown in Fig. 9. The HBM-based calculation results are shown as lines. A direct integration based on the Runge–Kutta (RK) method is performed to verify the accuracy of the HBM-based method. In the numerical integration, the swept frequency processes are performed in both the forward and the backward directions, and the vibration amplitudes of the payload in the steady-state responses (equaling to the displacement transmissibility) are shown as scatters in Fig. 9. The frequency responses calculated with two methods well coincide in most cases.

As shown in Fig. 9a, with $c = 0.2$, the displacement transmissibility of the isolator with the symmetric structure is smaller than 1 for all the frequencies. Thus, a full-band isolation is achieved. For the isolator with the parallel structure, a full-band isolation is impossible due to the nonzero linear stiffness. As shown in Fig. 9b, with $c = 0.16$, the vibrations are effectively isolated with the frequency exceeds a threshold. Compared with the parallel structure, the isolator with the symmetric structure exhibits a smaller resonant peak and a lower frequency threshold for the effective isolation. As shown in Fig. 9c, with $c = 0.15$, jump phenomena occur in the nonlinear isolators. The jump-down frequency of the isolator with the symmetric structure is lower. Furthermore, as shown in Fig. 9d, for the symmetric structure, only the odd harmonics are nonzero. For the parallel structure, the even harmonics are nonzero. Typically, the nonzero zero-order harmonic indicates that the equilibrium location changes with the frequency during vibration, and it is not contained in the amplitude-frequency responses in Fig. 9a– c. Besides, with the parallel structure, the HBM-based method results in an unstable response within $0.4 < \eta < 0.7$, while the numerical integration exhibits a peak. According to the stability analysis based on the Floquet theory, the eigenvalue of the monodromy matrix leaves the unit circle through − 1. It indicates the occurrence of a symmetry-breaking bifurcation due to the even-order harmonics [51]. In conclusion, the nonlinear isolators perform much

Table 2 Dimensions of the three-section beams

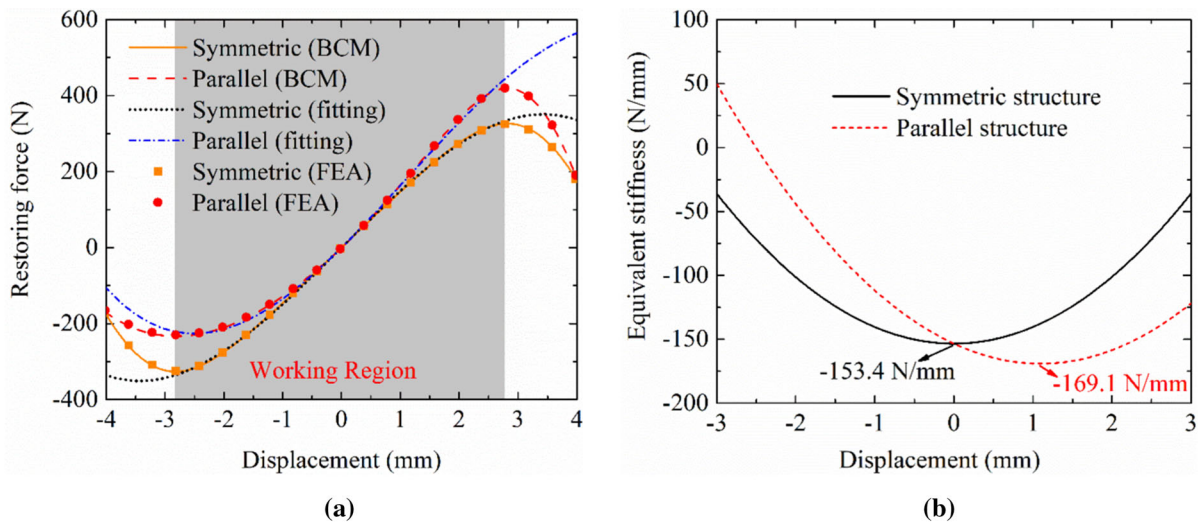| L_1	L_2	L_3	T_1	T_2	T_3	W	$\alpha_1 = \alpha_2 = \alpha_3$
35 mm	30 mm	35 mm	1.5 mm	5 mm	1.5 mm	10 mm	$\pi/52$ (-$\pi/52$)

Fig. 8 **a** The restoring forces and **b** the equivalent stiffness of the compliant mechanisms

Table 3 The stiffness parameters of the isolators

	K_s	k_1	k_2	k_3
Symmetric structure	153.4 N/mm	0	0	2.83×10^{-2}
Parallel structure	169.1 N/mm	0.102	-9.33×10^{-2}	2.83×10^{-2}
Linear isolator	153.4 N/mm	1	0	0

better than the linear isolator within the working region. Compared with the parallel structure, the isolator with the symmetric structure achieves better isolation performances with smaller resonant peak, broader isolation frequency band and fewer nonzero harmonics.

4.2 Structures of the isolators

For a comprehensive understanding for the functions of the compliant mechanism and the wire ropes in vibration isolation, three isolators are compared and shown in Fig. 10. The first one is the isolator with both the compliant mechanism and the wire ropes. For a comparison between the hysteretic damping and the linear damping, an isolator with the compliant mechanism and a linear damper is presented as the second isolator. To study the functions of the compliant mechanism, an isolator with the wire ropes, a linear spring and a linear damper is presented as the third isolator.

The dimensions of the compliant mechanism and the identified parameters of the wire ropes are shown in Tables 2 and 1, respectively. The characteristic

stiffness and the excitation amplitude are $K_{c-} = 153.4$ N/mm and $A_e = 1$ mm, respectively. The dimensionless parameters of three isolators are shown in Table. 4. The selected linear damping leads to similar resonant amplitudes of three isolators, and thus the isolation frequency and the isolation efficiency can be compared.

The generalized equivalent stiffness and the generalized equivalent damping ratio are calculated through Eqs. (26) and (30). As shown in Fig. 11a, the introduction of the compliant mechanism leads to quasi-zero initial stiffness, and the stiffness increases with an increasing displacement. The introduction of the wire ropes results in a raise of the initial stiffness, while the raise decreases exponentially with an increasing displacement. Besides, the wire ropes leads to slight increases of the linear and the cubic stiffness. Therefore, the isolators with only the compliant mechanism and only the wire ropes exhibit hardening and softening characteristics, respectively. The isolators with both the compliant mechanism and the wire ropes exhibit softening–hardening characteristics. Specifically, the equivalent stiffness decreases exponentially with small displacements and increases in a
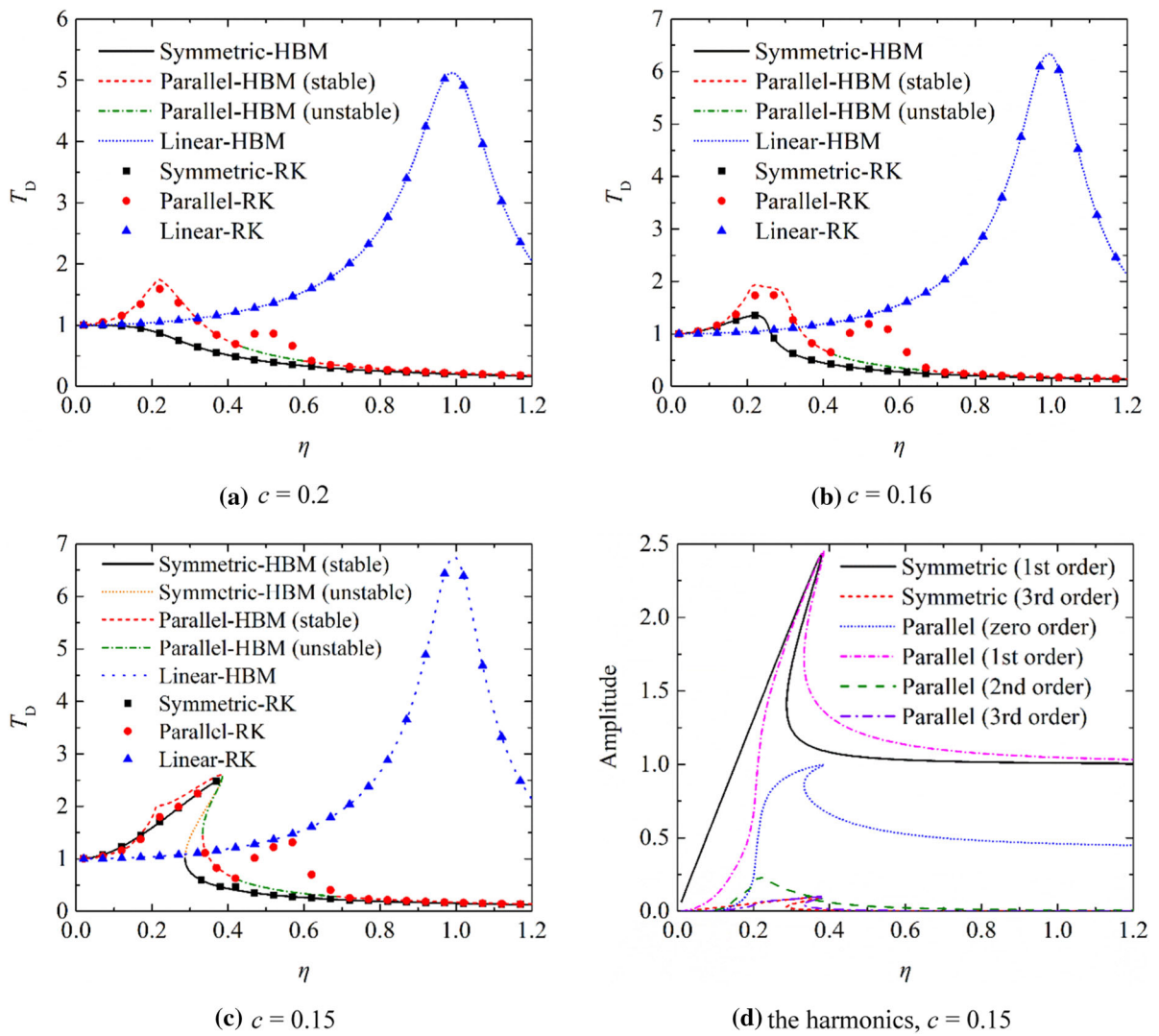
Fig. 9 The frequency responses of the isolators with **a** $c = 0.2$, **b** $c = 0.16$ and **c** $c = 0.15$, and **d** the frequency responses of different harmonics with $c = 0.15$
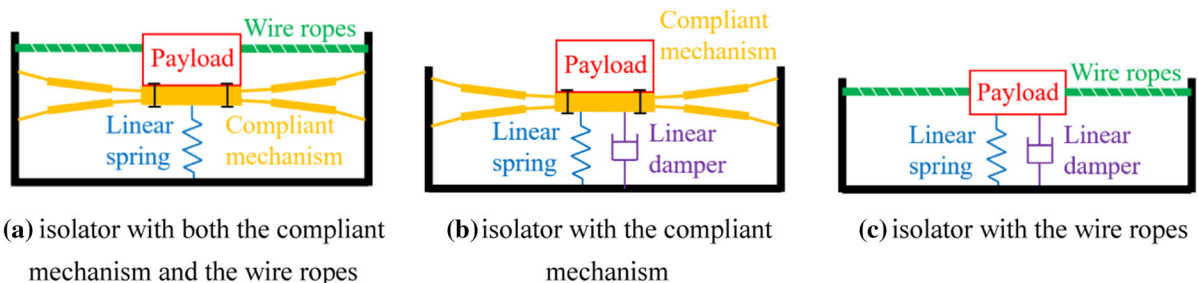

Fig. 10 Isolators with different nonlinear components: **a** both the compliant mechanism and the wire ropes, **b** only the compliant mechanism and **c** only the wire ropes

Table 4 The dimensionless parameters of the isolators with different components

Isolator structure	k_1	k_3	δ	β	γ	c
Figure 10a	0.072	2.88×10^{-2}	1.114	4.57	0.87	0
Figure 10b	0	2.83×10^{-2}	0	0	0	0.159
Figure 10c	1.072	0.05×10^{-2}	1.114	4.57	0.87	1
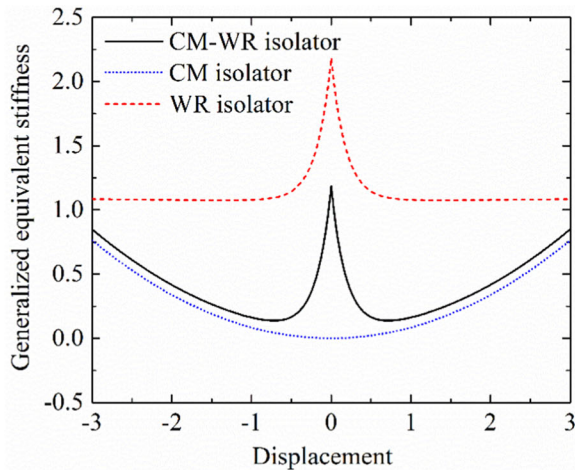
(a) Generalized equivalent stiffness
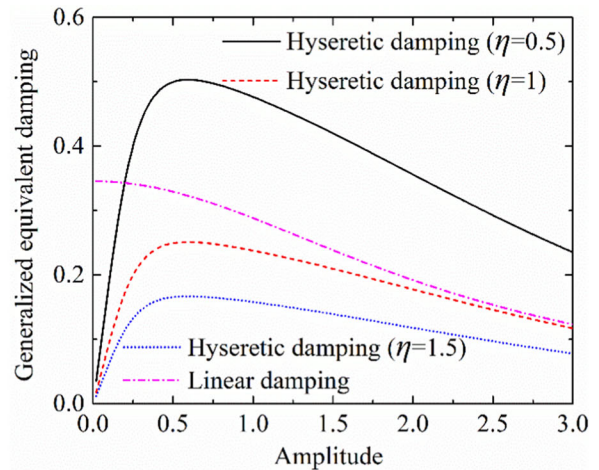
(b) Generalized equivalent damping ratio

Fig. 11 a The generalized equivalent stiffness and **b** the generalized equivalent damping ratio of the isolators ("CM-WR isolator" denotes the isolator with both the compliant mechanism and the wire ropes. "CM isolator" denotes the isolator with the compliant mechanism. "WR isolator" denotes the isolator with the wire ropes.)

quadratic relation with large displacements, as shown in Eq. (26).

The generalized equivalent damping ratio is related to the stiffness characteristics of the isolator. To compare the hysteretic damping resulted from the wire ropes and the linear damping, the damping effects are applied on nonlinear isolators with the same linear and cubic stiffness. The results are shown in Fig. 11b. The damping ratio of the linear damping decreases with the increasing amplitude, and it is independent with the frequency. The damping ratio of the hysteretic damping increases and then decreases with the increasing amplitude, because the wire ropes causes the stiffness softening for small amplitudes. Furthermore, the dissipated energy in one period (E_d) is independent with the frequency, and thus the equivalent damping ratio has an inverse proportion to the frequency as shown in Eq. (30).

The frequency responses of the isolators are shown in Fig. 12. The HBM-

based results coincide with the RK-based numerical results. Compared with the isolator with only the wire ropes, the isolator with both the compliant mechanism and the wire ropes exhibits a lower resonant frequency and thus a broader frequency band for vibration isolation. It is due to the HSLDS characteristics produced by the compliant mechanism. Compared with the isolator with only the compliant mechanism, the isolator with both the compliant mechanism and the wire ropes increases the resonant frequency and improves the isolation efficiencies at high frequencies. It is because the hysteretic damping results in a small equivalent damping ratio at high frequencies, which is beneficial for high-frequency isolation.

5 Parameter analysis

The stiffness characteristics of the compliant mechanism depend on the dimensions, and the thickness of
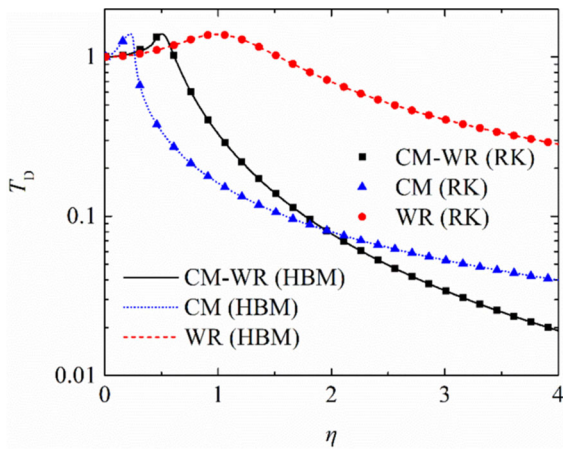
Fig. 12 The frequency responses of the isolators with different components ("CM-WR" denotes the isolator with both the compliant mechanism and the wire ropes. "CM" denotes the isolator with the compliant mechanism. "WR" denotes the isolator with the wire ropes.)

the two thin beams $T_{1,3}$ and the tilting angle of the three-section beam $\alpha_{1,2,3}$ are the key parameters. With $T_{1,3}$ determined, the stroke with negative stiffness (working stroke) increases with an increasing tilting angle. However, the increase of $\alpha_{1,2,3}$ is constrained by the allowable stress of the beam. Figure 13 shows the maximum value of $\alpha_{1,2,3}$ and the corresponding maximum working stroke with determined $T_{1,3}$, and the allowable stress is 800 MPa. The other dimensions are shown in Table 2. It can be seen that both the maximum tilting angle and the maximum working stroke decrease with the increase of the thickness. Thus, thin beams are more preferred to achieve larger
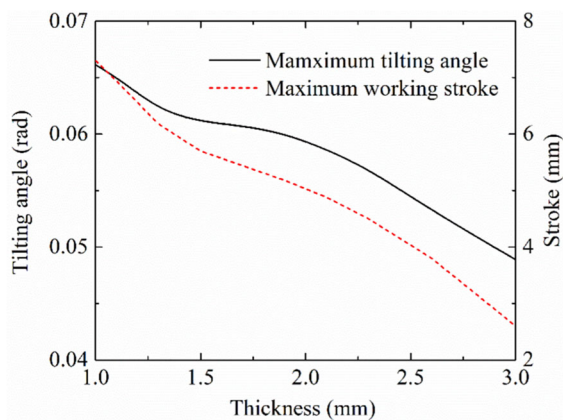

Fig. 13 The maximum tilting angle and the maximum working stroke of the compliant mechanism

working stroke. However, the allowable thickness is constrained by the machining capacity.

The compliant mechanisms with 4 groups of dimensions are adopted in the isolator with both the compliant mechanism and the wire ropes. The stiffness of the linear springs equals the absolute value of the initial negative stiffness of the compliant mechanisms. The determined and calculated parameters of the isolators are shown in Table 5. The other dimensions are the same with those in Table 2, and the other dimensionless parameters are the same with those in Table 4. It can be seen that K_s, which indicates the static load capacity of the isolator, decreases with decreasing $T_{1,3}$ and decreasing $\alpha_{1,2,3}$. The cubic stiffness k_3 decreases with decreasing $T_{1,3}$ and increasing $\alpha_{1,2,3}$.

The generalized equivalent stiffness and the frequency responses of the nonlinear isolators with different dimensions of the compliant mechanisms are shown in Fig. 14. For the isolators with larger cubic stiffness, the equivalent stiffness increases more dramatically with large displacements. The frequency responses of the isolators are similar at low frequencies. However, the isolator with larger cubic stiffness exhibits larger resonant amplitude and higher resonant frequency. It can be concluded that the dimensions of the compliant mechanisms affect the isolation performances through cubic stiffness, and smaller cubic stiffness is more preferred.

In conclusion, smaller thickness of the beams leads to larger working stroke, better vibration isolation performances but weaker load capacity. Larger titling angle results in larger working stroke, better vibration isolation performances and stronger load capacity. The upper limit of the tilting angle is constrained by the allowable stress of the beams.

6 Conclusions

This work proposes a nonlinear vibration isolator via a compliant mechanism with the negative stiffness and wire ropes with the hysteretic damping. The restoring force of the compliant mechanism is modelled based on a beam constraint model, and the force model is substantially validated by the finite element analysis. The hysteretic restoring force of the wire ropes is characterized with a Bouc–Wen model-based semi-physical model with the identified parameters. The

Table 5 The parameters of the isolators with different dimensions of the compliant mechanisms

$T_{1,3}$	$\alpha_{1,2,3}$	Maximum stress	Working stroke	K_s	k_3
1.5 mm	$\pi/52$	785 MPa	5.64 mm	153.4 N/mm	2.88×10^{-2}
1.1 mm	$\pi/49$	783 MPa	6.82 mm	70.2 N/mm	3.83×10^{-3}
1.1 mm	$\pi/52$	716 MPa	6.30 mm	69.3 N/mm	5.30×10^{-3}
1.1 mm	$\pi/65$	498 MPa	4.68 mm	64.4 N/mm	1.70×10^{-2}
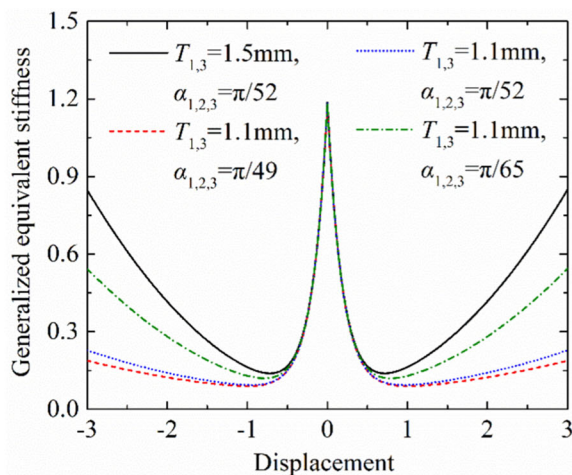
(a) generalized equivalent stiffness
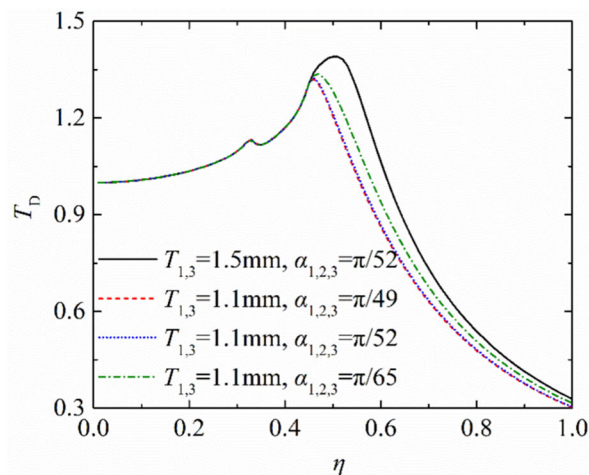
(b) frequency responses

Fig. 14 **a** The generalized equivalent stiffness and **b** the frequency responses of the isolators with different dimensions of the compliant mechanisms

dynamic model of the nonlinear isolator includes a polynomial function and an implicit differential function. The frequency responses are obtained through a harmonic balance-based semi-analytical method, and verified by a direct integration with a Runge–Kutta method. The generalized equivalent stiffness and the generalized equivalent damping ratio are defined for systems with multiple nonlinearities.

The investigation yields the following conclusions: (1) The compliant mechanism exhibits negative stiffness in a limited stroke. The isolator with the compliant mechanism demonstrates lower resonant frequency and smaller resonant amplitude. (2) The isolator with the symmetric compliant mechanism presents full-band isolation, stable response with a resonant peak and jump phenomenon with large, medium and small damping. The symmetric compliant mechanism is more preferred than the parallel compliant mechanism for broad-band vibration isolation. (3) The wire ropes increase the initial value of the generalized equivalent stiffness, and the generalized

equivalent damping ratio of the hysteretic damping has an inverse proportional relation with the frequency. Therefore, the introduction of the wire ropes enhances the isolation efficiencies at high frequencies at the cost of a higher resonant frequency. (4) The isolator with both the compliant mechanism and the wire ropes exhibits multiple nonlinearities. The incorporation of the HSLDS and the hysteretic damping is beneficial for a broad-band and high-efficient vibration isolation. (5) The working stroke and the vibration isolation performances can be improved by decreasing the thickness and increasing the tilting angle of the compliant mechanism. However, the decrease of the thickness weakens the load capacity, and the increase of the tilting angle is constrained by the allowable stress of the beam.

Declarations

References

1. Lu, Z.Q., Gu, D.H., Ding, H., Lacarbonara, W., Chen, L.Q.: Nonlinear vibration isolation via a circular ring. Mech. Syst. Signal Process. **136**, 106490 (2020)

2. Ding, H., Chen, L.Q.: Nonlinear vibration of a slightly curved beam with quasi-zero-stiffness isolators. Nonlinear Dyn. **95**(3), 2367–2382 (2019)

3. Zhang, Y.W., Lu, Y.N., Zhang, W., Teng, Y.Y., Yang, H.X., Yang, T.Z., Chen, L.Q.: Nonlinear energy sink with inerter. Mech. Syst. Signal Process. **125**, 52–64 (2019)

4. Hu, F., Jing, X.: A 6-DOF passive vibration isolator based on Stewart structure with X-shaped legs. Nonlinear Dyn. **91**(1), 157–185 (2018)

5. Shen, Y., Peng, H., Li, X., Yang, S.: Analytically optimal parameters of dynamic vibration absorber with negative stiffness. Mech. Syst. Signal Process. **85**, 193–203 (2017)

6. Li, H., Li, Y., Li, J.: Negative stiffness devices for vibration isolation applications: a review. Adv. Struct. Eng. **23**(8), 1739–1755 (2020)

7. Carrella, A., Brennan, M.J., Kovacic, I., Waters, T.P.: On the force transmissibility of a vibration isolator with quasi-zero-stiffness. J. Sound Vib. **322**(4–5), 707–717 (2009)

8. Wang, X., Liu, H., Chen, Y., Gao, P.: Beneficial stiffness design of a high-static-low-dynamic-stiffness vibration isolator based on static and dynamic analysis. Int. J. Mech. Sci. **142–143**, 235–244 (2018)

9. Lu, Z., Brennan, M.J., Chen, L.Q.: On the transmissibilities of nonlinear vibration isolation system. J. Sound Vib. **375**, 28–37 (2016)

10. Wang, Y., Li, S., Neild, S.A., Jiang, J.Z.: Comparison of the dynamic performance of nonlinear one and two degree-of-freedom vibration isolators with quasi-zero stiffness. Nonlinear Dyn. **88**(1), 635–654 (2017)

11. Gatti, G.: Statics and dynamics of a nonlinear oscillator with quasi-zero stiffness behaviour for large deflections. Commun. Nonlinear Sci. Numer. Simul. **83**, 105143 (2020)

12. Liu, X., Huang, X., Hua, H.: On the characteristics of a quasi-zero stiffness isolator using Euler buckled beam as negative stiffness corrector. J. Sound Vib. **332**(14), 3359–3376 (2013)

13. Fulcher B. A., Shahan D. W., Haberman M. R., Seepersad C. C., Wilson P. S.. Analytical and experimental investigation of buckled beams as negative stiffness elements for passive vibration and shock isolation systems. J. Vib. Acoust.; 136(3): 031009.

14. Huang, X., Liu, X., Sun, J., Zhang, Z., Hua, H.: Vibration isolation characteristics of a nonlinear isolator using euler buckled beam as negative stiffness corrector: a theoretical and experimental study. J. Sound Vib. **333**(4), 1132–1148 (2014)

15. Niu, F., Meng, L., Wu, W., Sun, J., Zhang, W., Meng, G., Rao, Z.: Design and analysis of a quasi-zero stiffness isolator using a slotted conical disk spring as negative stiffness structure. J. Vibroeng. **16**(4), 1769–1785 (2014)

16. Yan, L., Xuan, S., Gong, X.: Shock isolation performance of a geometric anti-spring isolator. J. Sound Vib. **413**(443), 120–143 (2018)

17. Cheng, C., Li, S., Wang, Y., Jiang, X.: On the analysis of a high-static-low-dynamic stiffness vibration isolator with time-delayed cubic displacement feedback. J. Sound Vib. **378**, 76–91 (2016)

18. Zhou, J., Xiao, Q., Xu, D., Ouyang, H., Li, Y.: A novel quasi-zero-stiffness strut and its applications in six-degree-of-freedom vibration isolation platform. J. Sound Vib. **394**, 59–74 (2017)

19. Shi, X., Zhu, S.: Simulation and optimization of magnetic negative stiffness dampers. Sens. Actuators, A **259**, 14–33 (2017)

20. Wang, K., Zhou, J., Ouyang, H., Cheng, L., Xu, D.: A semi-active metamaterial beam with electromagnetic quasi-zero-stiffness resonators for ultralow-frequency band gap tuning. Int. J. Mech. Sci. **176**, UNSP105548 (2020)

21. Howell, L.L., Magleby, S.P., Olsen, B.M.: Handbook of Compliant Mechanisms. Wiley, West Sussex, UK (2013)

22. Gatti, G.: A K-shaped spring configuration to boost elastic potential energy. Smart Mater. Struct. **28**, 077002 (2019)

23. Xu, Q.: Design of a large-stroke bistable mechanism for the application in constant-force micropositioning stage. J. Mech. Robot. **9**(1), 011006 (2016)

24. Han, Q., Huang, X., Shao, X.: Nonlinear kinetostatic modeling of double-tensural fully-compliant bistable mechanisms. Int. J. Non-Linear Mech. **93**, 41–46 (2017)

25. Zhao, H., Zhao, C., Ren, S., Bi, S.: Analysis and evaluation of a near-zero stiffness rotational flexural pivot. Mech. Mach. Theory **135**, 115–129 (2019)

26. Chen, G., Ma, F., Hao, G., Zhu, W.: Modeling large deflections of initially curved beams in compliant mechanisms using chained beam constraint model. J. Mech. Robot. **11**(1), 011002 (2019)

27. Bai, R., Awtar, S., Chen, G.: A closed-form model for nonlinear spatial deflections of rectangular beams in intermediate range. Int. J. Mech. Sci. **160**, 229–240 (2019)

28. Gao, R., Li, M., Wang, Q., Zhao, J., Liu, S.: A novel design method of bistable structures with required snap-through properties. Sens. Actuators, A **272**, 295–300 (2018)

29. Zhao, J., Zhang, J., Wang, K.W., Cheng, K., Wang, H., Huang, Y., Liu, P.: On the nonlinear snap-through of arch-shaped clamped–clamped bistable beams. J. Appl. Mech. **87**(2), 1–5 (2020)

30. Hao, G.: A framework of designing compliant mechanisms with nonlinear stiffness characteristics. Microsyst. Technol. **24**(4), 1795–1802 (2018)

31. Chen, Q., Zhang, X., Zhang, H., Zhu, B., Chen, B.: Topology optimization of bistable mechanisms with maximized differences between switching forces in forward and backward direction. Mech. Mach. Theory **139**, 131–143 (2019)

32. Lu, Z.Q., Brennan, M., Ding, H., Chen, L.Q.: High-static-low-dynamic-stiffness vibration isolation enhanced by

damping nonlinearity. Sci. China Technol. Sci. **62**(7), 1103–1110 (2019)

33. Kiani, M., Amiri, J.V.: Effects of hysteretic damping on the seismic performance of tuned mass dampers. Struct. Design Tall Spec. Build. **28**(1), 1555 (2019)

34. Moradpour, S., Dehestani, M.: Optimal DDBD procedure for designing steel structures with nonlinear fluid viscous dampers. Structures **22**, 154–174 (2019)

35. Wang, G., Wang, Y., Yuan, J., Yang, Y., Wang, D.: Modeling and experimental investigation of a novel arc-surfaced frictional damper. J. Sound Vib. **389**, 89–100 (2017)

36. Barbieri, N., Barbieri, R., Silva, R.A., Mannala, M.J., Barbieri, L.S.V.: Nonlinear dynamic analysis of wire-rope isolator and Stockbridge damper. Nonlinear Dyn. **86**(1), 501–512 (2016)

37. Gerges, R.R., Vickery, B.J.: Design of tuned mass dampers incorporating wire rope springs: Part I: dynamic representation of wire rope springs. Eng. Struct. **27**(5), 653–661 (2005)

38. Carpineto, N., Lacarbonara, W., Vestroni, F.: Hysteretic tuned mass dampers for structural vibration mitigation. J. Sound Vib. **333**(5), 1302–1318 (2014)

39. Carboni, B., Lacarbonara, W., Auricchio, F.: Hysteresis of multiconfiguration assemblies of nitinol and steel strands: experiments and phenomenological identification. J. Eng. Mech. **141**(3), 04014135 (2015)

40. Carboni, B., Lacarbonara, W., Brewick, P.T., Masri, S.F.: Dynamical response identification of a class of nonlinear hysteretic systems. J. Intell. Mater. Syst. Struct. **29**(13), 2795–2810 (2018)

41. Leblouba, M., Rahman, M.E., Barakat, S.: Behavior of polycal wire rope isolators subjected to large lateral deformations. Eng. Struct. **191**, 117–128 (2019)

42. Zhang, Y., Xu, K., Zang, J., Ni, Z., Zhu, Y., Chen, L.: Dynamic design of a nonlinear energy sink with NiTiNOL-steel wire ropes based on nonlinear output frequency response functions. Appl. Math. Mech. **40**(12), 1791–1804 (2019)

43. Zheng, L.H., Zhang, Y.W., Ding, H., Chen, L.Q.: Nonlinear vibration suppression of composite laminated beam embedded with NiTiNOL-steel wire ropes. Nonlinear Dyn. **103**, 2391–2407 (2021)

44. Awtar, S., Sen, S.: A generalized constraint model for two-dimensional beam flexures: nonlinear load-displacement formulation. J. Mech. Design **132**(8), 081008 (2010)

45. Casini, P., Vestroni, F.: Nonlinear resonances of hysteretic oscillators. Acta Mech. **229**(2), 939–952 (2018)

46. Niu, M.Q., Chen, L.Q.: Dynamic effect of constant inertial acceleration on vibration isolation system with high-order stiffness and Bouc–Wen hysteresis. Nonlinear Dyn. **103**, 2227–2240 (2021)

47. Yuan, T.C., Yang, J., Chen, L.Q.: A harmonic balance approach with alternating frequency/time domain progress for piezoelectric mechanical systems. Mech. Syst. Signal Process. **120**, 274–289 (2019)

48. Wong C. W., Ni Y. Q., Lau S. L. (1994) Steady-state oscillation of hysteretic differential model. I: response analysis. J. Eng. Mech.; 120(11): 2271–2298.

49. Lacarbonara, W.: Nonlinear Structural Mechanics-Theory, Dynamic Phenomena and Modeling. Springer, New York (2013)

50. Huang, J.L., Su, R.K.L., Chen, S.H.: Precise Hsu's method for analyzing the stability of periodic solutions of multi-degrees-of-freedom systems with cubic nonlinearity. Comput. Struct. **87**(23–24), 1624–1630 (2009)

51. Malatkar, P., Nayfeh, A.H.: Steady-state dynamics of a linear structure weakly coupled to an essentially nonlinear oscillator. Nonlinear Dyn. **47**, 167–179 (2007)